

Unravelling the unusually curved X-ray spectrum of RGB J0710+591 using *AstroSat* observations

Pranjupriya Goswami^{1*}, Atreyee Sinha², Sunil Chandra³, Ranjeev Misra⁴,
Varsha Chitnis⁵, Rupjyoti Gogoi¹, Sunder Sahayanathan^{6,7}, C. S. Stalin⁸,
K. P. Singh⁹, and J. S. Yadav¹⁰

¹*Department of Physics, Tezpur University, Napaam - 784028, India.*

²*AstroParticule et Cosmologie, Université Paris Diderot, CNRS/IN2P3, CEA/Irfu, Observatoire de Paris, Sorbonne Paris Cité, 10, rue Alice Domon et Léonie Duquet, 75205 Paris Cedex 13, France.*

³*Centre for Space Research, North-West University, Potchefstroom, 2520, South Africa.*

⁴*Inter-University Center for Astronomy and Astrophysics, Post Bag 4, Ganeshkhind, Pune - 411007, India.*

⁵*Tata Institute of Fundamental Research, Homi Bhabha Road, Colaba, 400 005 Mumbai, India.*

⁶*Astrophysical Sciences Division, Bhabha Atomic Research Centre, Mumbai - 400085, India.*

⁷*Homi Bhabha National Institute, Mumbai 400094, India*

⁸*Indian Institute of Astrophysics, Block II, Koramangala, Bangalore-560034, India.*

⁹*Indian Institute of Science Education and Research, Mohali, Knowledge city, Sector 81, SAS Nagar, Manauli, Punjab - 140306. India.*

¹⁰*Department of Physics, Indian Institute of Technology, Kanpur 208016, India.*

ABSTRACT

We report the analysis of simultaneous multi-wavelength data of the high energy peaked blazar RGB J0710+591 from the LAXPC, SXT and UVIT instruments on-board *AstroSat*. The wide band X-ray spectrum (0.35 – 30 keV) is modelled as synchrotron emission from a non-thermal distribution of high energy electrons. The spectrum is unusually curved, with a curvature parameter $\beta_p \sim 6.4$ for a log parabola particle distribution, or a high energy spectral index $p_2 > 4.5$ for a broken power-law distribution. The spectrum shows more curvature than an earlier quasi-simultaneous analysis of *Swift*-XRT/*NuSTAR* data where the parameters were $\beta_p \sim 2.2$ or $p_2 \sim 4$. It has long been known that a power-law electron distribution can be produced from a region where particles are accelerated under Fermi process and the radiative losses in acceleration site decide the maximum attainable Lorentz factor, γ_{max} . Consequently, this quantity decides the energy at which the spectrum curves steeply. We show that such a distribution provides a more natural explanation for the *AstroSat* data as well as the earlier XRT/*NuSTAR* observation, making this as the first well constrained determination of the photon energy corresponding to γ_{max} . This in turn provides an estimate of the acceleration time-scale as a function of magnetic field and Doppler factor. The UVIT observations are consistent with earlier optical/UV measurements and reconfirm that they plausibly correspond to a different radiative component than the one responsible for the X-ray emission.

Key words: galaxies: active – BL Lacertae objects: individual: RGB J0710+591 – X-rays: galaxies

* E-mail: pranjupriya.g@gmail.com

1 INTRODUCTION

Non-thermal emission observed from BL Lac class of AGNs are essentially dominated by emission from the relativistic jet which is directed towards the observer with a small angular separation. It is observationally featured by rapid variability from Doppler-boosted emission over a wide range of wavelengths from radio to γ -rays (Blandford & Rees 1978; Urry & Padovani 1995). The spectral energy distribution (SED) of BL Lacs is double peaked, and this unfolds information on the various physical processes and origins to the non-thermal emission from the jet. The low energy component includes radio – X-ray emission and is well understood to be synchrotron emission from a relativistic electron distribution (Ghisellini & Maraschi 1989). However, the origin of the high energy component from X-ray – very high energy (VHE) γ -ray emission is still unclear. It is generally modelled as inverse Compton (IC) radiation by the same electron population accounted for the synchrotron emission, or external photon field from the broad line region (BLR) and the accretion disc (leptonic models, Bloom & Marscher (1996)). This may also be due to hadronic interactions between accelerated protons & electron-positron pair or muon cascades (hadronic models, Boettcher (2010)).

The synchrotron peak in high energy peaked blazars (HBLs) typically lies in UV – X-ray energies and the hard X-ray spectrum shows a steep spectra (Baloković et al. 2016; Bartoli et al. 2016). Besides this, the X-ray spectrum also shows smooth curvature around the peak and a mild curvature in the falling part for certain HBL sources. The X-ray curvature possibly indicates an energy dependence of the particle acceleration probability, which results in a log-parabola type particle distribution (Massaro et al. 2004). Alternatively, an energy-dependent electron diffusion can also explain this curvature at hard X-ray energies (Goswami et al. 2018). It is often observed that the synchrotron peak shifts towards higher energy X-ray energies during flaring episodes in the range from few eV to few tens of keV and is evident in many sources, e.g., Mkn421 (Tramacere et al. 2009; Sinha et al. 2015), Mkn 501 (Pian et al. 1998), and 1ES 2344+514 (Giommi et al. 2000).

Interestingly, certain HBLs are known to have exceptionally high synchrotron peak even during their quiescent states. Costamante et al. (2001) initiated an extensive study on 5 BL Lac type sources with BeppoSAX observations covering a wide range of energy 0.1-100 keV. For four sources the peaks were estimated at hard X-ray energy 1-5 keV and for 1ES 1426+428, the synchrotron peak appeared at energy above 100 keV with a flat power law spectrum ($\alpha < 1$). Later, a few other sources are also observed to show this extreme synchrotron peak and consistently their Compton peak can reach up to 100 -200 GeV with hard very high energy (VHE) spectrum e.g, RGB J0710+591 (Acciari et al. 2010), 1ES 0347-121 (Aharonian et al. 2007). These high energy peaked sources are often termed as extreme high energy peaked BL Lacs (EHBLs).

RGB J0710+519 ($z=0.125$) is an EHBL, first discovered by *HEAO* A-1 and subsequently detected in VHE γ -rays with VERITAS array of atmospheric Cherenkov telescope during 2008 December and 2009 March (Ong 2009). The preliminary studies on this source indicate the spectral hardening at TeV energies and the extreme Compton behaviour

(Nieppola et al. 2006; Abdo et al. 2009). The spectral behaviour of this source has been studied by Acciari et al. (2010) for synchrotron and Compton spectral components using VHE γ -ray observation by VERITAS, supplemented with the multi-wavelength observations from *Fermi* and *Swift*. The time averaged *Swift*-XRT spectra during 20 February - 2 March, 2009 can be explained by an absorbed power-law model with photon index ~ 1.86 . This spectral hardening in X-ray spectrum is the indication that the synchrotron peak can reach up to 10 keV or above. A comprehensive study on this object and a few other extreme TeV BL Lacs involving more recent observations has been carried out by Costamante et al. (2018). The authors discussed the X-ray spectrum using the simultaneous *Swift* and *NuSTAR* observations and, interestingly, the synchrotron peak for this source was constrained for the first time at energy ~ 3.5 keV. In addition, the authors modelled the complete SED with various multi-wavelength data from *Fermi* satellite and other available data in the energy range extending from radio to VHE γ -rays. The optical/UV emission of this source is clearly not an extrapolation of the X-ray spectrum and a possible interpretation could be that different regions are responsible for X-ray and UV/optical emissions (Acciari et al. 2010; Costamante et al. 2018).

In this work, we perform a detailed investigation of the extreme synchrotron behaviour of the BL Lac source RGB J0710+591, and establish the nature of X-ray spectrum using strictly simultaneous multi-waveband *AstroSat* data for the first time. Our aim is to constrain the synchrotron peak within the limit of observed X-ray energies and study the particle acceleration mechanisms responsible for the curved synchrotron spectrum. The *AstroSat* data is supplemented with the simultaneous *Swift*-XRT and *NuSTAR* observations in energy range 0.3 – 79 keV to compare the spectral transitions during different flux states. Furthermore, we discuss the UV and optical emissions observed by the UV/optical instruments of *AstroSat* and *Swift*. The observations and data reduction procedures are described in section 2 and 3. In section 4, we perform spectral analysis. The interpretation of the results is discussed in Section 5.

2 ASTROSAT OBSERVATIONS

AstroSat, India's first multi-wavelength space observatory launched in September 2015, has five scientific instruments onboard covering a wide range of energies from UV to hard X-ray (Agrawal 2006; Singh et al. 2014; Rao et al. 2016). The instruments onboard *AstroSat* are: Soft X-ray focusing Telescope (SXT), Large Area X-ray Proportional Counters (LAXPC), UltraViolet Imaging Telescope (UVIT), Cadmium Zinc Telluride Imager (CZTI) and Scanning Sky Monitor (SSM). RGB J0710+591 was observed by SXT (as primary instrument), LAXPC and UVIT on 19 November, 2016 for 1 pointing (Obs ID: A02_085T02_9000000808; Table 1). The observations and data reduction techniques are discussed in the following sections 2.1, 2.2 and 2.3.

2.1 SXT

The SXT is a focusing telescope capable of X-ray imaging and spectroscopy in the energy range 0.3 – 8.0 keV

with 2' angular resolution and FOV of $\sim 40'$ diameter (Singh et al. 2016, 2017). The Level-1 SXT data observed in the photon counter (PC) mode were first processed with `sxtpipeline` available in the SXT software (*AS1SXTLevel2*, version 1.4b). The pipeline calibrates the source events and extracts Level-2 cleaned event files for the individual orbits. The cleaned event files of all the 10 orbits are then merged into a single cleaned event file using `SXTEVTMERGER` tool developed by the instrument team to avoid the time-overlapping events from the consecutive orbits. The `XSELECT` (V2.4d) package built-in *HEASOFT* is used to extract the source spectrum from the processed Level-2 cleaned event files. We selected the source region as a circular region of 14 arcmin radius centred at the source position, which encompasses more than 90% of the source pixels. The background spectrum "SkyBkg_comb_EL3p5_C1_Rd16p0_v01.pha", a composite product using a deep blank sky observation, distributed by the instrument team is used for spectral analysis. We have made use of the ancillary response file (ARF) "sxt_pc_exc100_v04_20190608.arf" (version 4.0) released recently by the instrument team. The used response file ("sxt_pc_mat_g0to12.rmf"), ARF and background are available at the SXT POC website¹. The source spectrum was then grouped using the `grppha` tool to ensure a minimum of 60 counts per bin. We obtained the net count rate for the SXT spectrum with 0.26 ct/s in the energy range 0.3 – 7.0 keV.

2.2 LAXPC

The LAXPC is one of the primary instruments on board *AstroSat* and consists of three identical co-aligned X-ray proportional counter units providing with high time resolution ($\sim 10 \mu\text{s}$) covering 3 – 80 keV energy band (Yadav et al. 2016; Antia et al. 2017; Agrawal et al. 2017; Misra et al. 2017). The proportional counter units are named as LAXPC10, LAXPC20 and LAXPC30 with each detector having an effective area of $\sim 2000 \text{ cm}^2$. To process the Level-1 LAXPC data, the *laxpc_soft* packages were used which is based on Fortran codes developed by the instrument team, available at the *AstroSat* Science Support Cell (ASSC) website². The data reduction procedures involve the generation of event files, standard GTI files of good time intervals to avoid Earth occultation and the South Atlantic Anomaly, and finally, extraction of source spectrum. To perform these, we used tools `laxpc_make_event` and `laxpc_make_stdgti` which are in-built in the *laxpc_soft* package. Data from source free sky regions observed within a few days of the source observation are used to generate and model the background and appropriate scaling is performed depending on the orbit. Finally, to generate the lightcurve and spectra, `laxpc_make_lightcurve` and `laxpc_make_spectra` tools were used. For the faint sources like AGNs, the background estimation is not straightforward, as the background starts dominating over the source counts. Therefore, the background was estimated from 50–80 keV counts where background seems relatively steady. The

data of each LAXPC unit (LAXPC10 and 20) is reduced separately and data from the top layers (layer 1) from each units are recommended to use for faint sources. LAXPC30 data were not considered due to the continuous gain shift observed in this unit, suspected to be caused by a gas leakage (Antia et al. 2017), while the data from LAXPC10 unit were unstable. Thus, in this analysis, we have only used the LAXPC data from LAXPC20. Using a total of 67.3 ks of useful data from the top layer of LAXPC20 (LX20-L1) the total count rate was estimated to be 0.5 ct/s in the energy range 3.0–30 keV.

2.3 UVIT

UVIT is primarily an imaging telescope on board *AstroSat* and consists of 3 channels in visible and ultraviolet (UV): VIS (320–550 nm), NUV (200–300 nm) and FUV (130–180 nm) wavelengths provided with absolute spatial resolution (FWHM $< 1.8''$) images in a field of view $\sim 28'$ (Kumar et al. 2012; Annapurni et al. 2016; Tandon et al. 2017). The detail information on the detectors and the UVIT filters are available at the *AstroSat* UVIT website³. UVIT Level-1 data were processed with *UVIT Level-2 Pipeline* (Version 5.6), software accessible at ASSC website and data reduction procedures were followed as recommended in the manual provided with the software packages. The pipeline generates the full frame astrometry fits images for each filter in NUV and FUV channels separately which are corrected for flat-fielding and drift due to rotation. To extract the count from the fits images corresponding to each filter, aperture photometry was performed using *IRAF* (Image Reduction and Analysis Facility) software tool. An aperture of 50 pixels radius size was selected to do photometry which encompasses $\sim 98\%$ of the source pixels. The extracted counts were then converted into fluxes for each filter using the unit conversion as suggested by Tandon et al. (2017). The fluxes were then corrected for Galactic interstellar extinction (Fitzpatrick 1999) with the values of $A_B = 0.139$ and $E_{(B-V)} = 0.034$ taken from NED. We have used the UVIT data for 5 filters which contain 3 NUV (NUVB13, NUVB4 and NUVN2) and 2 FUV filters (BaF2 and Silica) (See Table 2).

3 SWIFT AND NUSTAR OBSERVATIONS

To compare the *AstroSat* results and study the evolution of X-ray spectrum during different flux states, various instrument data are taken into account. The source has been monitored by *Swift* and *NuSTAR* on a few occasions. The two *Swift* pointing (Obs ID: 00031356055, 00031356056) are contemporaneous with the *AstroSat* observations within a gap of ~ 10 days, however, these observations are discarded due to low count rates and nonavailability of simultaneous *NuSTAR* observations. Hence, for the completeness of this work we have repeated the analysis from previous studies Costamante et al. (2018) with *Swift*-XRT and *NuSTAR* observations from 2015. The details of the observations are reported in Table 1.

We collected *Swift* and *NuSTAR* archival data that

¹ www.tifr.res.in/astrosat_sxt

² <http://astrosat-ssc.iucaa.in/?q=sxtData>

³ <http://uvit.iap.res.in/>

Table 1. Details of the observations from various instruments of *AstroSat*, *Swift* and *NuSTAR* missions

Instrument	Observation ID	Observation date (dd-mm-yyyy)	Exposure (ks)	
SXT	A02_085T02_9000000808	19-11-2016 T00:59:28	20.25	
LAXPC-20	A02_085T02_9000000808	19-11-2016 T21:23:08	27.5	
Swift	00081693002	02-09-2015 T00:03:16	XRT 4.43	UVOT 4.49
NuSTAR	60101037004	01-09-2015 T12:11:08	26.4	

Table 2. *AstroSat*-UVIT filter details and the measured flux:

Filter Name (slot)	λ_0 (Å)	$\Delta\lambda$ (Å)	Exposure (ks)	Flux (10^{-12} erg cm $^{-2}$ s $^{-1}$)
FUV				
BaF2 (F2)	1541	380	5.35	2.36 ± 0.02
Silica (F5)	1717	125	6	2.26 ± 0.03
NUV				
NUVB13 (F3)	2447	280	3.8	2.01 ± 0.07
NUVB4 (F5)	1632	275	8.7	2.02 ± 0.18
NUVN2 (F6)	2792	90	6.6	2.00 ± 0.16

Note: λ_0 and $\Delta\lambda$ are the central wavelength and the effective band width of the filters. The given fluxes are corrected for the Galactic extinction.

are available in NASA's HEASARC interface ⁴. The standard data reduction procedures were followed to analyse the data from various instruments UVOT, XRT in *Swift* and *NuSTAR*. *Swift*-XRT (Burrows et al. 2005) data were processed with the *XRTDAS* software package (Version 3.0.0) built-in *HEASoft* (Version 6.22). The source was observed in photon counting (PC) mode and corrected for pile-up by excluding central 3-pixels in the source region as the initial source count rate was above 0.5 ct/s. *Swift*-UVOT (Roming et al. 2005) observations of 6 UV filters: U, V, B, UVW1, UVW2 and UVM2 in UV and optical wavelengths (Poole et al. 2008), were included in this study. The data from both the telescope FPMA and FPMB in *NuSTAR* (Harrison et al. 2013) were processed using the *NuSTAR-DAS* software package (Version 1.4.1). The details of step-wise data reduction procedure for *Swift*-XRT and *NuSTAR* data are discussed in Goswami et al. (2018).

4 SPECTRAL MODELS AND ANALYSIS

Previous studies confirm spectral breaks with a smooth curvature in the X-ray spectrum of this source and therefore, a simple power-law interpretation is not adequate. A broken power-law or a log-parabola distribution can possibly explain this. Several authors have reported the curvature prop-

erty for the combined *Swift*-XRT and *NuSTAR* observations using a log-parabola photon distribution (Acciari et al. 2010; Costamante et al. 2018; Pandey et al. 2018). The main focus of this work is to present the results from various X-ray instruments onboard *AstroSat* observed in 2016. This can give us an idea about the spectral variations of the source during various flux states.

The spectral fittings were performed for each observation from various instruments using *XSPEC* (Version 12.9.1) software package distributed with *HEASoft* (Arnaud 1996). The correction of galactic absorption was done by using *TBabs* model in *XSPEC*, considering the value of equivalent-hydrogen column density (N_H) fixed at 4.44×10^{20} cm $^{-2}$ and was kept fixed throughout the analysis. This value was estimated by online tool ⁵ developed by the LAB survey group (Kalberla et al. 2005). A best-fit nominal gain offset of 0.03 keV as determined using *gain fit* option with a fixed gain slope of 1 is used, as recommended by SXT instrument team. This significantly improves the fit statistics. Once best-fit gain parameters are decided, we have fixed these throughout the spectral fitting in order to save computation time while calculating the error bars and contours. To determine the relative cross-calibration uncertainties between two instruments, a multiplicative constant factor is used along with models and reported in Table 3. We use the X-ray observations corresponding to joint XRT (ID:

⁴ <https://heasarc.gsfc.nasa.gov/>

⁵ <https://heasarc.gsfc.nasa.gov/cgi-bin/Tools/w3nh/w3nh.pl>

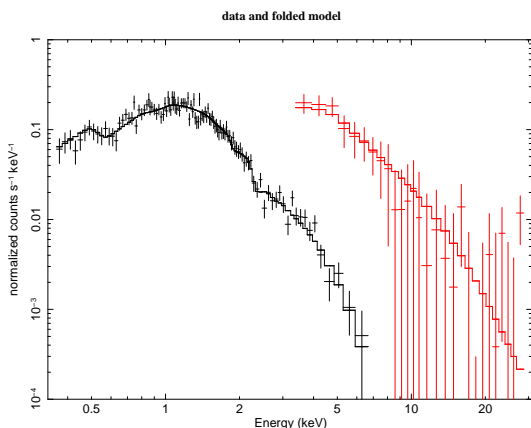


Figure 1. Figure shows combined SXT-LAXPC20 data (SXT in black and LAXPC in red) fitted with a log-parabola photon spectrum model.

00081693002) – *NuSTAR* in the energy range 0.35 – 50 keV and SXT – LAXPC in the range 0.35 – 30 keV for spectral fitting. Table 3 shows the X-ray spectral fitting results of these data sets using a log-parabola function in-built in *XSPEC*. The spectral fit and the residuals of the SXT-LAXPC data are shown in Figure 1. Both the spectra show clear curvatures, and the SXT observation alone can accommodate the synchrotron peak with a sharp spectral turnover. We observe a slight change in the 2-10 keV average flux which in contrast, shows a considerable change in the curvature value. The synchrotron peaks of both the spectra are estimated by log-parabola model and well constrained within the observed X-ray energy range. Interestingly, the peak shifts by a significant fraction (by a factor of ~ 3.5) during these epochs. In addition, we also observe a strong curvature in the X-ray spectrum of *AstroSat*-SXT, which is changed by 1.2 - 1.7 times from the previous XRT-*NuSTAR* spectrum. Hence, the spectral slope estimated at 1keV and 10keV using the best-fit log-parabola model parameters changes sharply in case of SXT-LAXPC spectrum (> 1.5) compared to XRT-*NuSTAR* spectrum (~ 1.07). This spectral steepening of SXT-LAXPC spectra is also consistent with the low energy spectral peak. The spectral fitting was performed by keeping the cross-normalization parameter free for the spectra corresponding to XRT and SXT and fixed at 1.0 for LAXPC-20 and *NuSTAR*. However, we observe that the cross-normalization between XRT and *NuSTAR* is too low and the difference is of the order of $\sim 40\%$. This is possibly due to the poor statistics of XRT data beyond 3 keV. Therefore, to keep this cross-normalization uncertainty under acceptable limit (typically $\lesssim 10 - 15\%$, Madsen et al. (2016)), we freeze this value at 0.85 for XRT. The change in χ^2 for other values of cross-normalization within 20%-15% for XRT observation are observed as 432.13 (429) for cross-normalization 0.80, 471.13 for 0.85, 486.27 for 0.90 and 518.57 for 0.95. Fixing the relative normalization causes marginal changes in curvature. Hence, for better understanding, we have reported the best-fit parameters for both the cases with the cross-normalization free and fixed at 0.85 for XRT.

It is clear from our spectral fitting results that the two X-ray spectra observed by XRT-*NuSTAR* and SXT-

LAXPC are significantly curved. The SXT-LAXPC spectrum appears to be more curved with steeper X-ray spectral index than XRT-*NuSTAR* spectrum when fitted with a log-parabola model. For a better understanding about the emitting particle distribution and the intrinsic curvature, we reproduce the synchrotron spectrum assuming various underlying electron distributions.

The synchrotron emissivity due to an electron distribution losing its energy in a magnetic field B is given by, (Rybicki & Lightman 1986),

$$j_{\text{syn}}(\nu) = \frac{1}{4\pi} \int P_{\text{syn}}(\gamma, \nu) N(\gamma) d\gamma \quad (1)$$

Here, $N(\gamma)$ is the electron number density at dimensionless energy γ and P_{syn} as the single particle synchrotron emissivity. Assuming a spherical emission region of volume V , the observed synchrotron flux $F_{\text{syn}}(\nu)$ after accounting for relativistic beaming and cosmological evolution will be, (Begelman et al. 1984),

$$F_{\text{syn}}(\nu) = \frac{\delta_D^3 (1+z)}{d_L^2} V j_{\text{syn}} \left(\frac{1+z}{\delta_D} \nu \right) \quad \text{erg cm}^{-2} \text{s}^{-1} \text{Hz}^{-1}, \quad (2)$$

Here, z is the redshift of the source, d_L is the luminosity distance and δ_D is the relativistic Doppler factor. The observed synchrotron spectral shape is determined by $N(\gamma)$ and hence different particle distribution or acceleration mechanism could possibly explain the observed X-ray spectral nature of this source in different flux states.

To interpret the X-ray spectral curvature, we refit the *AstroSat* and XRT-*NuSTAR* observations as synchrotron spectrum due to different electron distributions and adding it as a local model in *XSPEC*. We first assume a broken power-law distribution for $N(\gamma)$ given by,

$$N(\gamma)d\gamma = \begin{cases} K \gamma^{-p_1} d\gamma, & \gamma_{\text{min}} < \gamma < \gamma_b \\ K \gamma_b^{(p_2-p_1)} \gamma^{-p_2} d\gamma, & \gamma_b < \gamma < \gamma_{\text{max}} \end{cases} \quad (3)$$

where, γ_b is the break energy and p_1 and p_2 are two particle indices at low and higher energies. A broken power-law distribution is capable to fit both the spectra and the best-fit parameters are reported in Table 4. The parameter E_b is the break energy in the photon spectrum associated with the particle break energy γ_b . However, although the model shows reasonably good χ^2 fit statistics, the model is inappropriate to explain the SXT spectrum as it demands higher curvature. The model fit parameters are not constrained, showing a large interval in the error estimation ($p_2 > 4.5$).

In order to explain the higher curvature, we assume for $N(\gamma)$ a log-parabola particle distribution which is given by

$$N(\gamma)d\gamma = K \left(\frac{\gamma}{\gamma_0} \right)^{-\alpha_p - \beta_p \log(\gamma/\gamma_0)} d\gamma \quad (4)$$

Here, α_p the particle spectral index at energy γ_0 and β_p , representing the curvature are the free parameters. K is the normalization constant. A log-parabola particle distribution model is statistically a better model than a broken power-law distribution with since it involves a lesser number of parameters (see Table 4). The model parameters are better constrained in XRT-*NuSTAR* spectrum, but showing larger interval for SXT-LAXPC spectrum while estimating errors. The estimation of the error for each parameter in all the models is within 90% confidence range.

Table 3. Best-fit parameters using log-parabola photon spectrum model

Observation	Constant *	α	β	χ^2 (dof)	$E_{syn,peak}$ (keV)	$F_{0.3-2keV}$ (10^{-12} erg cm $^{-2}$ s $^{-1}$)	$F_{2-10keV}$ (10^{-12} erg cm $^{-2}$ s $^{-1}$)
SXT – LAXPC-20	1.09	1.82 $^{+0.07}_{-0.07}$	0.64 $^{+0.18}_{-0.17}$	111.15 (135)	1.37 $^{+0.16}_{-0.13}$	8.53 $^{+0.12}_{-0.07}$	7.03 $^{+0.53}_{-0.44}$
XRT – <i>NuSTAR</i>	0.59	1.58 $^{+0.07}_{-0.07}$	0.38 $^{+0.04}_{-0.05}$	394.81 (428)	3.63 $^{+0.34}_{-0.35}$	6.79 $^{+0.10}_{-0.17}$	10.01 $^{+0.06}_{-0.07}$
	0.85	1.28 $^{+0.05}_{-0.05}$	0.51 $^{+0.04}_{-0.03}$	457.31 (429)	5.01 $^{+0.21}_{-0.22}$	6.78 $^{+0.16}_{-0.14}$	13.51 $^{+0.13}_{-0.12}$

Note: * The relative cross-normalization constant between two different X-ray instruments. The best-fit values for combined XRT-*NuSTAR* spectrum are reported here correspond to the cross-normalization constant for SXT free and fixed at 0.85, while fixed at 1.0 for *NuSTAR*. This parameter was kept at 1.0 for LAXPC and free for SXT observations in SXT-LAXPC20 spectrum. The errors are estimated within 90% confidence range based on the criterion used in *XSPEC*.

These results point out the exceptional curved feature of the SXT-LAXPC spectrum with unconstrained high energy index $p > 4.5$ in broken power-law and a large value of spectral curvature $\beta_p \sim 6.4$ in log-parabola particle distributions. In spite of good χ^2 fit estimations, these models do not have a reasonable explanation to validate the unusual curvature in SXT-LAXPC spectrum. Further, this is consistent with the sharp spectral change witnessed in the photon spectra (Table 3); however, the change in the slope is more prominent in case of particle distribution. For XRT-*NuSTAR* spectrum the change in the slope of the particle distribution corresponding to emission at 1keV and 10keV is ~ 3.9 . On the other hand, this slope change in case of SXT-LAXPC spectrum is ~ 8 , which is almost twice that of XRT-*NuSTAR*. This ensures the curvature in *AstroSat* X-ray spectrum is considerably higher than that of XRT-*NuSTAR*.

Alternatively, a steep spectral curvature can be an outcome of rapidly decaying particle distribution near the maximum available electron energy γ_{max} . To model this, we consider a scenario where the electrons are accelerated through Fermi acceleration process at the vicinity of a shock (Acceleration region, AR) and undergo synchrotron energy losses. The electron distribution $N(\gamma)$ in the AR will be governed by (Kardashev 1962),

$$\frac{d}{d\gamma} \left[\left(\frac{\gamma}{t_a} - A\gamma^2 \right) N(\gamma) \right] + \frac{N(\gamma)}{t_e} = Q_0 \delta(\gamma - \gamma_0) \quad (5)$$

Where, t_a and t_e are the acceleration and the escape time scales, $A\gamma^2$ decides the radiative loss term and for simplicity we consider a monoenergetic electron injection with energy γ_0 into AR. The steady state solution in AR for constant t_a and t_e will then be (Kirk et al. 1998),

$$N(\gamma)d\gamma = K \left(\frac{\gamma}{\gamma_{max}} \right)^{-p} \left(1 - \frac{\gamma}{\gamma_{max}} \right)^{(p-2)} d\gamma \quad (6)$$

Here, $p = \left(1 + \frac{t_a}{t_e} \right)$ is the particle spectral index. The maximum energy of the electron attained in AR will be decided by the rate of acceleration and radiative loss, $\gamma_{max} = \frac{1}{At_a}$. The radiative loss term A, in equation 5 is associated with the intrinsic magnetic field and given by,

$$A = \frac{4}{3} \frac{\sigma_T}{m_e c} \left(\frac{B^2}{8\pi} \right) \quad (7)$$

Where, σ_T the Thomson cross-section. We convolve the number density given by equation 6 with the single particle emissivity to obtain the synchrotron spectrum which is incorporated as a local model in *XSPEC*. The particle spectral index, p and the synchrotron photon energy E_{max} corresponding to γ_{max} are chosen as model parameters.

The model shows satisfactory fits and the best-fit values of model parameters are tabulated in Table 4. Figure 2 shows the model spectral fit and the corresponding fit residuals for SXT-LAXPC (LHS) and XRT-*NuSTAR* (RHS) observations. The parameters are well constrained within a small interval. This is indeed a remarkable result that the change in X-ray shapes can be interpreted in terms of a maximum Lorentz factor γ_{max} in the acceleration zone that varies significantly over time. This model provides a more natural explanation to the observed spectral evolution and particularly the sharp curvature seen by SXT. The photon energy corresponds to γ_{max} for both the spectra are well confined and can be estimated within the observation range.

The best fit E_{max} let us to estimate the maximum available electron energy in AR, with the knowledge of source magnetic field and Doppler factor

$$\gamma_{max} = 4.02 \times 10^6 \left(\frac{\delta_D}{30} \right)^{-1/2} \left(\frac{B}{0.011} \right)^{-1/2} \left(\frac{E_{max}}{54.76} \right)^{1/2} \quad (8)$$

Here, the choice of B and δ_D is chosen from Costamante et al. (2018). We estimate the γ_{max} for XRT-*NuSTAR* spectrum as 4.02×10^6 using the best-fit parameter $E_{max}=54.76$ (keV) for XRT cross-normalization 0.85. The estimated γ_{max} changes by a factor 1.08, when we consider the XRT cross-normalization as 0.59. Since γ_{max} is decided by the acceleration and radiative cooling timescales, using equation 7 and 8, t_a will be,

$$t_a = 1.59 \times 10^6 \left(\frac{\delta_D}{30} \right)^{1/2} \left(\frac{B}{0.011} \right)^{-3/2} \left(\frac{E_{max}}{54.76} \right)^{-1/2} \text{secs} \quad (9)$$

The estimation of γ_{max} and t_a from above equations demands prior knowledge of intrinsic magnetic field and Doppler factor. Unfortunately, this information can not be attained only from the *AstroSat* observation and demand information at γ -ray energies. In reality, we expect to see significant changes in the magnetic field for different epochs, and hence the acceleration time scale. Thus, we conclude that the observed spectral transition is associated

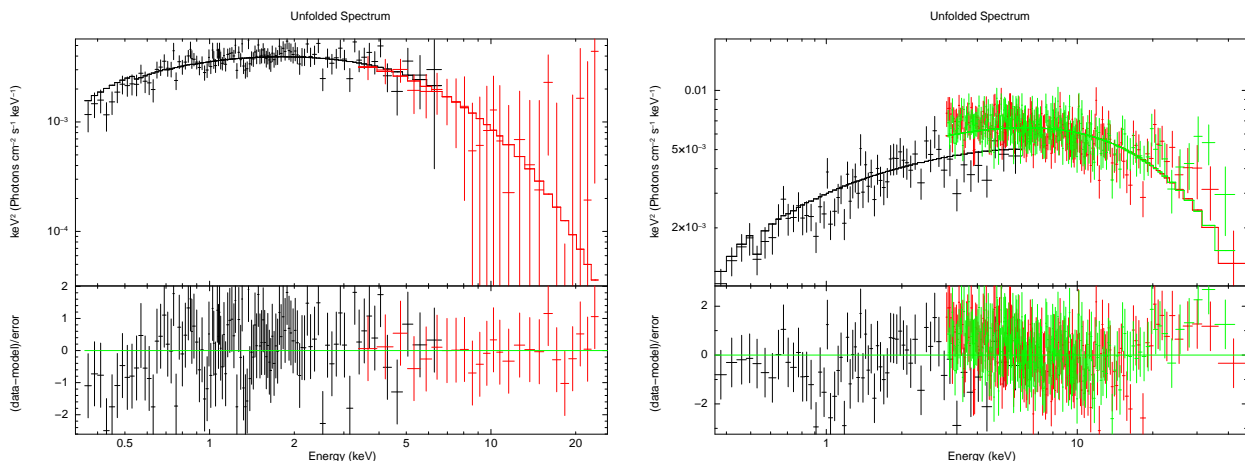


Figure 2. Figures show spectral fitting for combined SXT-LAXPC20 observations on LHS (SXT in black and LAXPC in red) and the simultaneous XRT and NuSTAR observation on RHS (Constant=0.85, XRT in black and the NuSTAR data from FPMA and FPMB are in red and green) using PL with γ_{max} model.

Table 4. Best-fit parameters using synchrotron spectrum models with broken power-law, log-parabola and PL with γ_{max} particle distributions. The best-fit parameters correspond to the XRT-NuSTAR spectrum are reported for both the cases with XRT cross-normalization free and fixed at 0.85.

Observation	SXT – LAXPC-20				XRT – NuSTAR				
Broken	p1	p2	E_b (keV)	χ^2 (dof)	Const.	p1	p2	E_b (keV)	χ^2 (dof)
Power-law	< 2.02	> 4.5	2.44 ^{+0.44} _{-1.28}	110.42 (134)	0.59	1.49 ^{+0.37} _{-0.70}	3.88 ^{+0.24} _{-0.16}	2.77 ^{+0.79} _{-0.76}	390.57 (427)
					0.85	<0.59	4.60 ^{+0.51} _{-0.23}	3.25 ^{+1.30} _{-0.20}	463.82 (428)
Log-parabola	α_p	β_p	χ^2 (dof)		Const.	α_p	β_p	χ^2 (dof)	
	1.96 ^{+0.38} _{-0.61}	6.41 ^{+4.35} _{-2.51}	110.35 (135)		0.59	1.73 ^{+0.25} _{-0.29}	2.17 ^{+0.40} _{-0.35}	395.37 (428)	
					0.85	0.40 ^{+0.29} _{-0.34}	3.67 ^{+0.51} _{-0.45}	471.13 (429)	
PL with γ_{max}	p	E_{max} (keV)	χ^2 (dof)		Const.	p	E_{max} (keV)	χ^2 (dof)	
	2.01 ^{+0.21} _{-0.01}	10.36 ^{+0.98} _{-0.72}	111.74 (135)		0.59	2.25 ^{+0.11} _{-0.10}	65.12 ^{+1.52} _{-1.24}	423.00 (428)	
					0.85	2.11 ^{+0.11} _{-0.11}	54.76 ^{+0.96} _{-0.86}	440.96 (429)	

with the variation in acceleration time scale or the magnetic field/Doppler factor over time.

Further, the *AstroSat* UVIT observation in the near-far UV energy ranges (4-8 eV) shows an irregular shape and is clearly not an extrapolation of the X-ray spectrum. Figure 3 shows the broad optical/UV to X-ray SEDs of *AstroSat* and *Swift*-NuSTAR observations. This result agrees with the previous ones shown by Acciari et al. (2010) and Costamante et al. (2018) using UVOT observations. Costamante et al. (2018) demonstrated this prominent extra thermal component along with optical flux points and concluded that the optical/UV emission is a separate component from a different emission origin. The work has the complete illustration of the SED modelling, using a giant elliptical galaxy template from Silva et al. (1998) to resolve the discrepancy seen in optical/UV regime. The far-IR emission from WISE data seems to be consistent with being due to the host galaxy contribution, which may belong to the same spectral component as optical/UV. We see a marginal difference in the UV fluxes between observations in 2016 with UVIT and 2015 with UVOT, by a factor ~ 1.5 . Note that X-ray fluxes vary significantly during the period while the UV counterpart is relatively steady (see Table 2). This is a

further evidence that both X-ray and UV emissions belong to separate emission origins.

5 SUMMARY AND DISCUSSION

The unprecedented true simultaneous data from *AstroSat* in broad X-ray energy range are crucial to establish the exact nature of synchrotron spectrum of extreme high energy peaked BL Lac sources. Unfortunately, the X-ray spectral study in different flux states has not been reported due to the unavailability of simultaneous X-ray observations. With the advent of *AstroSat*, we are able to perform such a comparative study. The major aspects of the present work through spectral analysis are, 1) validate the exact location of synchrotron spectral peak within the observational range, 2) to interpret the variation in the multi-epoch X-ray spectra, and 3) verify the peculiar behaviour seen in optical/UV emissions using *AstroSat*-UVIT observations.

We investigate the X-ray spectrum of the EHLB source RGB J0710+591 for two different epochs, observed by SXT-LAXPC in November 2016 and XRT-NuSTAR in September 2015. The synchrotron peaks of these X-ray spectra are well

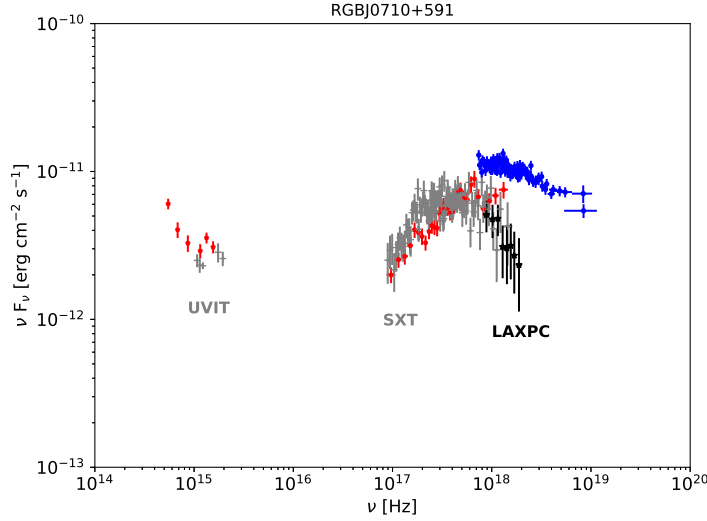


Figure 3. Figure shows the comparison between the SEDs with *AstroSat* (SXT,UVIT: grey, LAXPC: black) and combined *Swift* (XRT,UVOT: red) and *NuSTAR* (blue) observations from November 2016 and September 2015. The SEDs are clearly different in shape, showing more curvature in SXT spectrum. The change in UV fluxes is marginal.

confined at high energies within the observation range. The major outcome of this study is the observed sharp curvatures and the phenomenal change in the synchrotron peaks. The sharp curvature is better explained by the synchrotron spectrum associated with the decline of the underlying electron number density around the maximum attainable electron energy in the acceleration region. This enable us to estimate the maximum available electron energy γ_{max} in the blazar emission region and the acceleration timescale in terms of the source magnetic field and the Doppler factor. Consistently, the observed X-ray spectral evolution can be understood as a result of varying magnetic field/Doppler factor or with the particle acceleration time. The other important result is the optical/UV emissions observed with *AstroSat*-UVIT. These observations reconfirm the optical/UV spectrum corresponds to a different emission component other than X-ray.

An important constraint in estimating the maximum available electron energy and the associated acceleration time scale is the lack of knowledge related to the source magnetic field and the jet Doppler factor. In the present work, we have assumed these quantities to be same as the one estimated by [Costamante et al. \(2018\)](#) through broadband spectral modelling during September 2015. However, its been understood that the magnetic field and the jet Doppler factor often seem to vary during different flux states. This discrepancy can be overcome with the simultaneous information available at γ -ray energies. Further, the estimated γ_{max} can be cross checked through VHE observations.

Acknowledgements: This research has used the data of *AstroSat* mission of the Indian Space Research Organisation (ISRO), archived at the Indian Space Science Data Centre (ISSDC). The authors would like to acknowledge the support from the LAXPC Payload Operation Center(POC)

and SXT POC at the TIFR, Mumbai for providing support in data reduction. This work has been performed utilizing the calibration data-bases and auxillary analysis tools developed, maintained and distributed by *AstroSat*-SXT team with members from various institutions in India and abroad. The work has also made use of data, software, and/or web tools obtained from NASA's High Energy Astrophysics Science Archive Research Center (HEASARC), a service of the Goddard Space Flight Center and the Smithsonian Astrophysical Observatory. RM, RG and PG would like to thank the Indian Space Research organisation (ISRO), Department of Space, India for the grant under "Space Science Promotion". SC acknowledges CSR-NWU Potchefstroom, SA-GAMMA and NRF-South Africa for supporting his *AstroSat* & HESS related projects. PG would like to thank IUCAA and BARC for their hospitality.

REFERENCES

- Abdo A. A., et al., 2009, *ApJ*, **707**, 1310
 Acciari V. A., et al., 2010, *ApJ*, **715**, L49
 Agrawal P. C., 2006, *Advances in Space Research*, **38**, 2989
 Agrawal P. C., et al., 2017, *Journal of Astrophysics and Astronomy*, **38**, 30
 Aharonian F., et al., 2007, *A&A*, **473**, L25
 Annapurni S., et al., 2016, preprint, ([arXiv:1612.02535](#))
 Antia H. M., et al., 2017, *ApJS*, **231**, 10
 Arnaud K. A., 1996, in Jacoby G. H., Barnes J., eds, *Astronomical Society of the Pacific Conference Series Vol. 101*, *Astronomical Data Analysis Software and Systems V*. p. 17
 Baloković M., et al., 2016, *ApJ*, **819**, 156
 Bartoli B., et al., 2016, *ApJS*, **222**, 6
 Begelman M. C., Blandford R. D., Rees M. J., 1984, *Reviews of Modern Physics*, **56**, 255
 Blandford R. D., Rees M. J., 1978, *Phys. Scr.*, **17**, 265
 Bloom S. D., Marscher A. P., 1996, *ApJ*, **461**, 657
 Boettcher M., 2010, arXiv e-prints, p. [arXiv:1006.5048](#)
 Burrows D. N., et al., 2005, *Science*, **309**, 1833

- Costamante L., et al., 2001, *A&A*, **371**, 512
- Costamante L., Bonnoli G., Tavecchio F., Ghisellini G., Tagliaferri G., Khangulyan D., 2018, *MNRAS*, **477**, 4257
- Fitzpatrick E. L., 1999, Publications of the Astronomical Society of the Pacific, 111, 63
- Ghisellini G., Maraschi L., 1989, *ApJ*, **340**, 181
- Giommi P., Padovani P., Perlman E., 2000, *MNRAS*, **317**, 743
- Goswami P., Sahayanathan S., Sinha A., Misra R., Gogoi R., 2018, *MNRAS*, **480**, 2046
- Harrison F. A., et al., 2013, *ApJ*, **770**, 103
- Kalberla P. M. W., Burton W. B., Hartmann D., Arnal E. M., Bajaja E., Morras R., Pöppel W. G. L., 2005, *A&A*, **440**, 775
- Kardashev N. S., 1962, *Soviet Ast.*, **6**, 317
- Kirk J. G., Rieger F. M., Mastichiadis A., 1998, *A&A*, **333**, 452
- Kumar A., et al., 2012, in Space Telescopes and Instrumentation 2012: Ultraviolet to Gamma Ray. p. 84431N ([arXiv:1208.4670](https://arxiv.org/abs/1208.4670)), doi:10.1117/12.924507
- Madsen K. K., Beardmore A. P., Forster K., Guainazzi M., Marshall H. L., Miller E. D., Page K. L., Stuhlinger M., 2016, *The Astronomical Journal*, 153, 2
- Massaro E., Perri M., Giommi P., Nesci R., 2004, *A&A*, **413**, 489
- Misra R., et al., 2017, *ApJ*, **835**, 195
- Nieppola E., Tornikoski M., Valtaoja E., 2006, *A&A*, **445**, 441
- Ong R., 2009, The Astronomer's Telegram, 1941
- Pandey A., Gupta A. C., Wiita P. J., 2018, *ApJ*, **859**, 49
- Pian E., et al., 1998, *ApJ*, **492**, L17
- Poole T. S., et al., 2008, *MNRAS*, **383**, 627
- Rao A. R., Singh K. P., Bhattacharya D., 2016, preprint, ([arXiv:1608.06051](https://arxiv.org/abs/1608.06051))
- Roming P. W. A., et al., 2005, *Space Science Reviews*, 120, 95
- Rybicki G. B., Lightman A. P., 1986, *Radiative Processes in Astrophysics*
- Silva L., Granato G. L., Bressan A., Danese L., 1998, *ApJ*, **509**, 103
- Singh K. P., et al., 2014, in Space Telescopes and Instrumentation 2014: Ultraviolet to Gamma Ray. p. 91441S, doi:10.1117/12.2062667
- Singh K. P., et al., 2016, in Space Telescopes and Instrumentation 2016: Ultraviolet to Gamma Ray. p. 99051E, doi:10.1117/12.2235309
- Singh K. P., et al., 2017, *Journal of Astrophysics and Astronomy*, **38**, 29
- Sinha A., Shukla A., Misra R., Chitnis V. R., Rao A. R., Acharya B. S., 2015, *A&A*, **580**, A100
- Tandon S. N., et al., 2017, *AJ*, **154**, 128
- Tramacere A., Giommi P., Perri M., Verrecchia F., Tosti G., 2009, *A&A*, **501**, 879
- Urry C. M., Padovani P., 1995, *PASP*, **107**, 803
- Yadav J. S., et al., 2016, in Space Telescopes and Instrumentation 2016: Ultraviolet to Gamma Ray. p. 99051D, doi:10.1117/12.2231857

This paper has been typeset from a $\text{\TeX}/\text{\LaTeX}$ file prepared by the author.